

Low damped acoustic modes in polycrystalline nickel cavities fabricated by ps-laser delamination

Alba Viejo Rodríguez¹, Marco Gandolfi^{2,3,4}, Andrea Rossetti¹, Yoav Urbina Elgueta⁵, Evgeny B. Modin⁵, Svetlana Starikovskaia⁶, Tat Loon Chng⁶, Vasily Temnov⁶, Maria Antonietta Vincenti^{2,3,4}, Daniele Brida¹, Paolo Vavassori^{5,7}, and Nicolò Maccaferri^{8*}

¹Department of Physics and Materials Science, University of Luxembourg, 162a Avenue de la Faïencerie, 1511 Luxembourg, Luxembourg

²Dipartimento di Ingegneria dell'Informazione, Università degli Studi di Brescia, Via Branze 38, 25123 Brescia, Italy

³Consiglio Nazionale delle Ricerche - Istituto Nazionale di Ottica, Via Branze 45, 25123 Brescia, Italy

⁴Consorzio Nazionale Interuniversitario per le Telecomunicazioni (CNIT), Viale G.P. Usberti 181/A Sede Scientifica di Ingegneria-Palazzina 3, 43124 Parma, Italy

⁵CIC nanoGUNE, Tolosa Hiribidea, 76, 20018 Donostia-San Sebastián, Spain

⁶LSI, Ecole Polytechnique, CEA/DRF/IRAMIS, CNRS, Institut Polytechnique de Paris, 91128 Palaiseau, France

⁷IKERBASQUE Basque Foundation for Science, Plaza Euskadi 5, 48009 Bilbao, Spain

⁸Department of Physics, Umeå University, Linnaeus väg 24, 901 87 Umeå, Sweden

*nicolo.maccaferri@umu.se

ABSTRACT

Single-shot picosecond (ps) laser induced delamination allows for the direct generation of suspended membranes from a continuous metallic film. It is not known if polycrystalline membranes obtained by local ps-pulsed laser delamination of a continuous film on a substrate would show low damping compared to the film. Here, we report on the dynamics of acoustic waves excited by femtosecond light pulses and confined in a single freestanding nickel layer, acting as an acoustic cavity. By combining Fourier transform analysis of the measured pump-probe signal and numerical multi-physics simulations, we show that high-frequency (> 10 GHz) longitudinal acoustic pulses can resonate inside the cavity and display lower damping compared to a reference nickel film on SiO₂ substrate given that the conditions of total internal reflection are nearly met in the cavity, even if these cavities display more defects in terms of crystal structure and surface roughness. This result provides evidence that the ps-laser induced local delamination could be effectively utilized, after further optimization, as a flexible process to design on-demand micro-structured systems for opto-acoustic applications.

Opto-acoustic properties of materials^{1,2} can be exploited in a broad range of applications, for instance to modulate light intensity^{3,4}, control magnetization dynamics^{5,6}, gravitational wave detection and quantum opto-mechanics⁷, as well as ultrafast and all-optical switching^{8,9} and ultrasound detection techniques¹⁰ for the characterization of nanoscopic features in materials^{11,12}. Furthermore, elastic strain engineering uses stress to boost material properties¹³, including enhanced electron mobility in semiconductors for more efficient photovoltaic devices¹⁴ and transistors¹⁵. In mechanical engineering, the pursuit of resonators with low damping is pivotal for a broad range of applications, from ultralow noise opto-mechanical quantum technologies¹⁶ to energy efficient magneto-acoustics in spintronic devices^{17,18}. These perspectives led to studies of acoustic wave dynamics engineering to achieve lower damping, and increase the propagation properties of acoustic waves, for instance by removing the substrate^{6,19}. In connection to the latter strategy, it has recently been introduced a method, called laser delamination, to pattern cavities detached from the substrate and supporting a unique combination of multiple excitations (magnetic, optical, acoustic)²⁰⁻²². This process, if properly controlled, allows for the direct on-demand patterning of suspended membranes on areas down to the microscale, thereby enabling the development of opto-acoustic devices that would require very complex and time-consuming processing by using more conventional lithography techniques.

Here, we experimentally study large ($>10\ \mu\text{m}$) regions (bubbles) of freestanding nickel films and show that the damping is weaker in such cavities compared to films in contact with a SiO_2 substrate. Our work shows that the delaminated suspended Ni membrane indeed displays an effective damping lower than that of the unexposed film.

Freestanding nickel cavities were fabricated using a pulsed laser focused on 230 nm thick nickel thin film evaporated on top of a SiO_2 substrate. For laser fluence slightly (a few percent) below the ablation threshold it is possible to obtain the formation of closed delamination cavities²² (more details in Supplementary Note 1 and Supplementary Figure S1). From now on, the freestanding nickel cavity will be referred to as ‘cavity’ and the nickel film on top of the substrate not undergoing the delamination process used as reference sample, will be referred to as ‘film’. SEM images of both the film and a typical cavity produced by our method are presented in Figure 1a,b (details on sample preparation for SEM imaging can be found in Supplementary Note 2). In the inset in the right panel of Figure 1a, we can observe the coalescence of small crystal grains of the pristine film into large crystallites induced by the delamination process in the cavity, accompanied by an increase of the roughness of the backside nickel/air interface in the latter case.

To experimentally excite and probe the opto-acoustic response of both cavity and film we used a standard pump-probe scheme (more details can be found in Supplementary Note 3). In Figure 2a we show the transient reflectance curves measured under identical excitation conditions on both the cavity and the film. The generation of an acoustic mode traveling back and forth inside the samples results in the appearance of equidistantly separated echoes in both cases. The origin of such echoes is connected to the fact that the pump pulse, whose penetration is shorter than the thickness of the cavity and the film, heats up only the upper part of the system (the first 30 nm, approximately, corresponding to the optical skin depth of nickel at 515 nm). This localized heating

triggers longitudinal acoustic waves that travel towards the lower part of the nickel domain. When the acoustic pulse reaches the lower nickel/air (cavity) or nickel/SiO₂ (film) boundary, it is reflected to the first interface where the probe pulse detects the effect of the strain on the transient optical response of the system (see also Figure 1b). The periodicity of the echoes depends on the thickness of the cavity/film and the sound velocity in nickel.

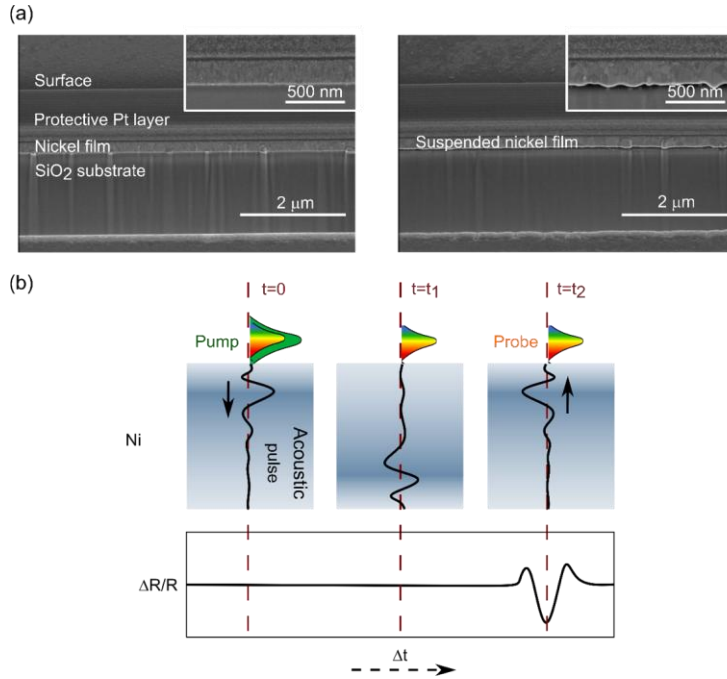


Figure 1. (a) SEM cross-sections cuts of the nickel film (left) and of one representative cavity (right). Insets: magnified image of the film and cavity cross-section. The protective Pt layer was used only for imaging purposes and not in the cavity that were measured. (b) Sketch of a differential reflectance ($\Delta R/R$) experiment where the opto-acoustic response dynamics is tracked as a function of pump-probe time delay (Δt). Upon arrival ($t=0$), the pump pulse thermally excites the sample. As a result, an acoustic pulse propagates throughout the nickel ($t=t_1$). After a round trip ($t=t_2$), the acoustic pulse comes back at the nickel/air interface and a change in the sample reflectance connected to the presence of such an echo can be detected within the probe signal, which typically contains additional information (e.g., an exponential decay factor connected to electron-electron and electron-phonon dynamics not discussed in this sketch).

Considering a thickness of 230 nm, and a sound velocity of longitudinal acoustic waves of 6.04 nm/ps²³, we can expect a periodicity for the roundtrip of 76 ps. This number matches the observed periodicity in the measured data for the film (see blue dots in Figure 2a,b). However, an approximately 3 ps shorter roundtrip time is observed for the cavity (see red dots in Figure 2a, b). This slight difference can arise partially from a little thinning of the nickel layer after the delamination process, although this difference is below the resolution of our SEM measurements. Additionally, and perhaps more significantly, the formation of large crystallites with a certain preferential crystal orientation could result in a slightly higher speed of sound in the cavity²⁴. We

speculate that in the film, the crystallites are much smaller than the relevant acoustic length-scale and the acoustic pulse travels in an effective medium where the speed of sound is mediated over all crystal directions resulting in a slightly slower effective propagation speed as compared to the cavity where this average over different crystalline directions might be less effective.

The exponential decay of the relaxation dynamics shown in Figure 2a can be attributed mainly to electron-electron and electron-phonon scattering in the time range accessed by our pump-probe experiments. We filtered out this contribution using an exponential fitting procedure. To account for potential experimental artifacts induced by the long delay lines in the experiment, we also included a polynomial correction in our baseline-removal algorithm with the aim of isolating the optically induced acoustic response (Figure 2b). For a scan of approximately 480 ps, five acoustic echoes are observed in the film, whereas an extra echo can be observed for the cavity (corresponding to 10 and 12 round trips, respectively). This finding suggests a weaker damping of the acoustic pulse in the cavity with respect to the film, which is a signature that the conditions of higher reflection at the backside nickel/air interface are met in the freestanding film. Nonetheless, it can be noticed in Figure 2b that the acoustic echoes in the cavity have a different shape and, during the first three round trips, are less intense in amplitude compared to the film case. The large size (comparable to the film thickness) of the crystallites in the cavity case, as well as their random orientation, can account for the larger modes' dispersion in the cavity. In addition, the process of formation of these larger grains results in a larger roughness of the freestanding cavity backside interface with air (especially that created by the separation from the SiO₂ induced by delamination), which should produce an attenuation of the acoustic modes, and the “broadness” of the strain profile as compared to the untreated reference film⁶. The comparison of the SEM cross sections of the cavity and the film (right and left panel of Fig. 1a, respectively) seem to support this explanation.

To further compare the opto-acoustic response of film and cavity, we performed a Fourier analysis of the experimental transient reflectance curves (see Figure 2c and 2d, respectively). In both cases we observe a series of peaks, corresponding to the different acoustic eigenmodes contributing to the acoustic wave-packet propagating in the two systems. We can distinguish six clear peaks for the case of the film and five for the cavity. Remarkably, the acoustic spectrum of the response of the cavity is clearly dominated by lower frequency modes compared to the film. This analysis is another way to see the “broadness” of the strain profile in the cavity compared to the film. The spectral position of these eigenmodes can be estimated by following a simple approach. The cavity can be modeled as a homogeneous nickel layer of thickness h with free external faces, and due to the symmetry of the excitation, only the longitudinal modes can be excited. The eigenfrequencies satisfy the relation²⁵:

$$f_n = \frac{v_l}{2h}n, \quad n = 1,2,3, \dots \quad (1)$$

where v_l is the longitudinal speed of sound. As for the film, it can be modelled as a nickel layer on top of a semi-infinite SiO₂ substrate. The nickel layer leaks out mechanical energy to the

substrate, hence the eigenfrequencies \tilde{f} are complex, their imaginary part representing the acoustic damping. Since the acoustic impedance of nickel ($Z_{Ni} = 5.37 \text{ kg m}^{-2}\text{s}^{-1}$) exceeds the one of the SiO_2 ($Z_{\text{SiO}_2} = 1.31 \text{ kg m}^{-2}\text{s}^{-1}$), the real part of the eigenfrequencies obeys to Equation (1) as well²⁶. The position of the eigenfrequencies is highlighted in Figure 2c, d with green asterisks and confirms that the observed eigenmodes are indeed longitudinal acoustic waves propagating inside cavity and film. A small offset between experimental Fast Fourier Transform (FFT) and calculated eigenmodes frequencies can be appreciated, which can be explained by considering the non-homogeneous speed of sound in the cavity due to the large crystallites and the interface irregularities generated by the fabrication process.

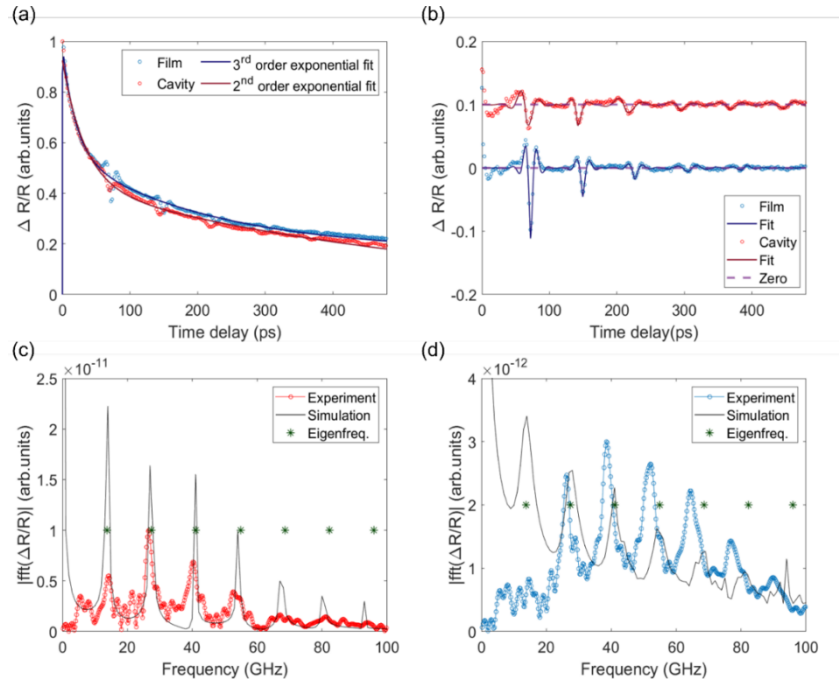


Figure 2. (a) Transient reflectance measurements of the film (blue dots) and the cavity (red dots) with a baseline exponential fit (continuous curves). (b) Transient reflectance signal after removing the baseline exponential decay to isolate the optically induced acoustic response (dots). As a guide for the eye, we fit each echo individually with a decaying sinusoidal. (c)-(d) Modulus of the Fourier transform spectrum of the experimental data of the cavity (c) and film (d). The asterisks represent the frequencies at which longitudinal acoustic eigenmodes are expected for the geometry considered here (air/nickel film/air or glass) and an ideal sound velocity of 6.04 nm/ps with a perfect homogeneous nickel film of thickness 220 nm. The continuous lines are the results from the numerical multiphysics simulations.

To further support our experimental results, we developed an opto-thermo-mechanical model, and solved it with FEM implemented in Comsol Multiphysics® (see Supplementary Note 4 for further details)²⁷⁻²⁹. Since the pump pulse at 515 nm illuminates from the top the nickel layer (we assume a fluence equal to 5 mJ/cm² as in the experiments) and penetrates for less than 30 nm (see Supplementary Figure S7), a localized electronic temperature increase in the nickel layer close to

the air side up to 800 K just after a pump pulse has interacted with the system (see also Supplementary Figure S8). The electrons deliver energy to the phonon population, and hence a phononic temperature increase occurs. On the air side of the Ni layer, the phononic temperature reaches 150 K approximately 2 ps after pump excitation (see Supplementary Figure S8). After 2 ps, a thermal expansion of the first 30 nm of the nickel layer takes place, triggering the generation of an acoustic pulse, which travels towards the backside of the Ni layer, and when it arrives on the second interface, it is reflected (see Supplementary Note 4).

The reflection is only partial in the case of the film, whereas the totality of the mechanical energy is reflected, in principle, at the bottom boundary of the cavity. This can be appreciated in the simulations where for the cavity we have an almost infinite number of echoes compared to the film where the echoes vanish quickly (see Supplementary Figure S9 and S10, respectively). After the reflection, a wavefront propagates towards the top part of the nickel layer and when it arrives in the first 30 nm of the layer – the zone interacting with the probe beam – a transient variation of the mechanical displacement (see Supplementary Note 4) due to the echo is recorded by the probe, changing the transient reflectance signal detected in our setup. The FFT transform of the longitudinal displacement calculated with FEM is reported in Figure 2c, d (continuous black lines), showing good qualitative agreement with the peaks of the probe signal FFT, and confirming the consistency of the model with the experimental data and observations. The minor discrepancies between the calculated eigenmodes and the experimental ones can be attributed to the idealized conditions assumed in our simulations, which are performed on an ideal system with the purpose of highlighting in a simple and transparent way the underlying physics. Specifically, we modeled a perfectly homogenous polycrystalline nickel film/cavity, while the actual system possesses defects, grains and surface irregularities. This also impacts the velocity of sound, which we can expect to be lower in systems with a high degree of defects³⁰. A model including inhomogeneities effects could improve the quantitative agreement between simulation and experiment. This goes, however, beyond the scope of this work. Instead, we emphasize that our sample already exhibits low-damped propagating acoustic pulses compared to the film case. In contrast with the simulations results, it is also worth mentioning that in our experiments the film does not display a peak at the fundamental frequency (defined as the inverse of the round-trip time of the acoustic pulse propagating in the cavity), around 15 GHz, that will correspond to the first eigenmode, which is indeed predicted by our model. This can be explained by zero detection efficiencies at certain frequencies resulting from the zero-overlap integral between the acoustic eigenmode and the photo-acoustic sensitivity function³¹.

To understand better the relative contributions of the eigenmodes to the pulse envelope propagating inside the cavity and the film, we performed also FFT of the single acoustic echoes. In more detail, we focused on the first five echoes and Fourier transformed them individually (see Figure 3 a, b; more details in Supplementary Note 5). In this way, we could extract information about the damping and amplitude of the propagating acoustic modes in both cases as function of frequency, as further discussed in the SI (see Figures S11 and S12).

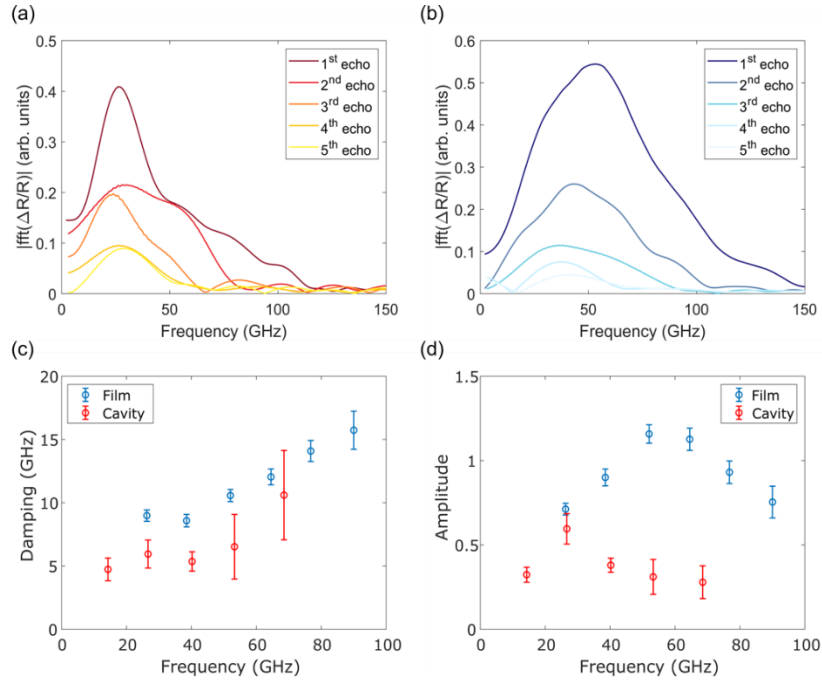


Figure 3. Modulus of the Fourier transform of the isolated first five acoustic echoes for the film (a) and cavity (b), respectively. (c) Damping as a function of frequency obtained from the Fourier transform analysis for the film (blue points) and cavity (red points). (d) Amplitude of the acoustic modes as a function of the frequency for film (blue points) and cavity (red points), extracted from the Fourier transform analysis.

Although the spectrum of the first echo of the cavity extends above 100 GHz, a reliable extraction of amplitude and damping of eigenmodes above 70 GHz was not possible due to the rapid attenuation of the higher echoes in that frequency range (see Figure 3b). Nonetheless, a clear difference can be observed when looking at the damping for film and cavity (see Figure 3c). In more detail, the damping in the cavity is weaker, confirming that more echoes should be observed in the pump-probe measurements due to higher internal reflectance of the acoustic envelope at the backside nickel/air interface. Low frequency modes contribute much more to the acoustic response in the case of the cavity, while high frequency modes (higher order eigenmodes) are instead contributing more to the carrier envelope in the film case (see Figure 3d). The fact that the strain pulse inside the film contains higher modes with higher weight agrees with the observation of a “narrower” profile in the time domain (compare the blue and red curves in Figure 2b). Furthermore, since higher modes dissipate more, they should last less. This is consistent with the fact that we have more round trips in the cavity as we have a spectrum with amplitudes peaking at lower frequencies (see Figure 3d). Noteworthy, the amplitude of the acoustic modes in the film is generally larger, further suggesting that the quality of the film is higher than that of the cavity. We speculate that the role of the roughness here might be dominant, creating jitter in the reflection, thus broadening of the pulses within the cavity, reducing their amplitude and shifting the dominant eigenmodes towards lower frequencies. Finally, it is worth mentioning that it has been shown previously³² that surface roughness results in the additional broadening of picosecond acoustic

pulses. The estimated surface roughness exceeding 10 nm at the bottom interface of laser-produced membranes (see Fig. 1a) results in the substantial inhomogeneous broadening of the observed acoustic echoes after each reflection. As such, it results in the conspicuous attenuation of acoustic pulses, notably of their high-frequency components. This observation appears to agree with experimental results in Fig. 2c and Fig. 3d. The combined effect of enhanced surface roughness and modified polycrystalline structure of the membranes seems to compensate the effect of “perfect” acoustic reflection from the bottom interface, as compared to the nickel/glass substrate. Overall, the frequency-domain analysis performed here corroborates the time-domain measurements.

In conclusion, we performed an ultrafast spectroscopy study of acoustic phonons excited by femtosecond light pulses and confined in a cavity of a freestanding nickel layer fabricated using laser delamination. By combining FFT analysis and numerical multi-physics simulations, we showed that the freestanding cavity detached from the substrate displays different acoustic response and a weaker damping compared to a reference thin film on a SiO₂ substrate, resulting in an overall low damping of the acoustic modes. This work provides evidence that a ps-laser-based approach towards the fabrication of opto-acoustic resonators is viable. As the next step, further efforts are needed to improve control over the microstructure and roughness of these membranes. Once this is achieved, we envision this type of structures and the ps-laser processing can become relevant to enable an easier and more flexible integration of such membranes in commercially available devices: for example, GHz-range RF filters employing suspended thin film acoustic resonators (often referred to as FBARs) are used in mobile phones and other communication devices, the only difference is that the fabrication is much easier. Finally, since these cavities are made of a magnetic material, they can represent an outstanding playground for studying multi-physics effects in magnetism, magneto-photonics, and magneto-acoustics³³.

ACKNOWLEDGEMENTS

N.M. acknowledges support from the Swedish Research Council (Grant No. 2021-05784), the Knut and Alice Wallenberg Foundation through the Wallenberg Academy Fellows Programme (Grant No. 2023.0089), the Wenner-Gren Foundations (Grant No. UPD2022-0074), and the European Research Council (Grant No. 101116253). A.V.R., D.B. and N.M. acknowledge support from the European Commission (Grant No. 964363) and the Luxembourg National Research Fund (Grant No. C19/MS/13624497). D.B. acknowledges support from the European Regional Development Fund (Project ‘UltrafastLux 2’ Grant No. 2023-01-04). Y.U.E. and P.V. acknowledge support from the Spanish Ministry of Science and Innovation under the Maria de Maeztu Units of Excellence Program (Grant No. CEX2020-001038-M) and Project No. PID2021-123943NB-I00 (OPTOMETAMAG), as well as by Predoctoral Fellowship No. PRE2022-103017 and the Research Program for International Talents at Ecole Polytechnique. M.A.V. and M.G. acknowledge financial support of MUR “CARMEL” project (CUP D73C24000220001).

REFERENCES

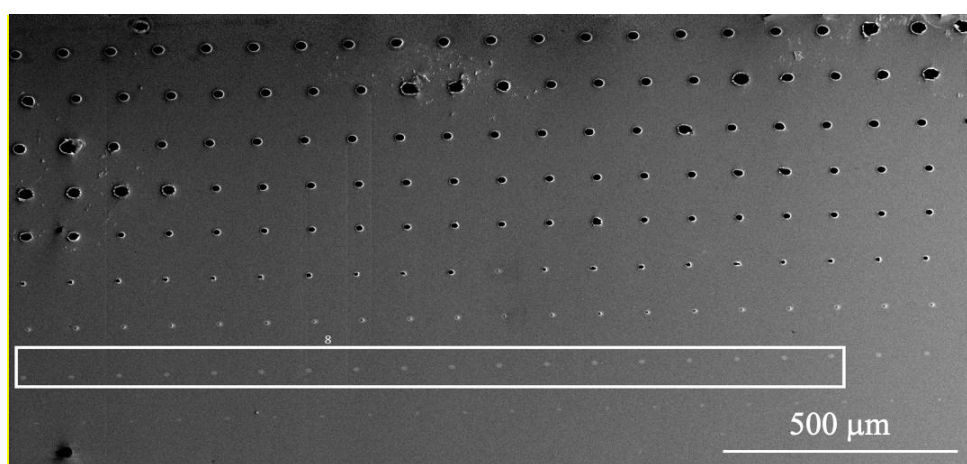
- ¹ Yu.E. Lozovik, and V.A. Sharapov, “Excitation of coherent acoustic phonons by a femtosecond pulse,” *Phys. Solid State* **45**(5), 969–971 (2003).
- ² H. Zhang, A. Antoncicchi, S. Edward, I. Setija, P. Planken, and S. Witte, “Unraveling Phononic, Optoacoustic, and Mechanical Properties of Metals with Light-Driven Hypersound,” *Phys. Rev. Applied* **13**(1), 014010 (2020).
- ³ J. Kuttruff, D. Garoli, J. Allerbeck, R. Krahn, A.D. Luca, D. Brida, V. Caligiuri, and N. Maccaferri, “Ultrafast all-optical switching enabled by epsilon-near-zero-tailored absorption in metal-insulator nanocavities,” *Communications Physics* **3**(1), (2020).
- ⁴ J. Kuttruff, R. Krahn, A. De Luca, V. Caligiuri, and N. Maccaferri, “Ultrafast opto-acoustic modulation of light reflectance in metal-insulator-metal epsilon-near-zero nanocavities,” in *Metamaterials XIII*, edited by V. Kuzmiak, P. Markos, and T. Szoplik, (SPIE, Online Only, Czech Republic, 2021), p. 41.
- ⁵ J.-W. Kim, M. Vomir, and J.-Y. Bigot, “Ultrafast Magnetoacoustics in Nickel Films,” *Phys. Rev. Lett.* **109**(16), 166601 (2012).
- ⁶ J.-W. Kim, and J.-Y. Bigot, “Magnetization precession induced by picosecond acoustic pulses in a freestanding film acting as an acoustic cavity,” *Phys. Rev. B* **95**(14), 144422 (2017).
- ⁷ N.J. Engelsens, A. Beccari, and T.J. Kippenberg, “Ultrahigh-quality-factor micro- and nanomechanical resonators using dissipation dilution,” *Nat. Nanotechnol.* **19**(6), 725–737 (2024).
- ⁸ A.N. Koya, J. Cunha, K.A. Guerrero-Becerra, D. Garoli, T. Wang, S. Juodkasis, and R. Proietti Zaccaria, “Plasmomechanical Systems: Principles and Applications,” *Advanced Functional Materials* **31**(41), 2103706 (2021).
- ⁹ A.N. Koya, M. Romanelli, J. Kuttruff, N. Henriksson, A. Stefancu, G. Grinblat, A. De Andres, F. Schnur, M. Vanzan, M. Marsili, M. Rahaman, A. Viejo Rodríguez, T. Tapani, H. Lin, B.D. Dana, J. Lin, G. Barbillon, R. Proietti Zaccaria, D. Brida, D. Jariwala, L. Veisz, E. Cortés, S. Corni, D. Garoli, and N. Maccaferri, “Advances in ultrafast plasmonics,” *Applied Physics Reviews* **10**(2), 021318 (2023).
- ¹⁰ G. Wissmeyer, M.A. Pleitez, A. Rosenthal, and V. Ntziachristos, “Looking at sound: optoacoustics with all-optical ultrasound detection,” *Light Sci Appl* **7**(1), 53 (2018).
- ¹¹ T.J. Grimsley, F. Yang, S. Che, G.A. Antonelli, H.J. Maris, and A.V. Nurmikko, “Ultrafast optoacoustics applied to the study of material nanostructures,” *J. Phys.: Conf. Ser.* **278**, 012037 (2011).
- ¹² Y. He, G. Luo, J. Huang, Y. Li, H. Sohn, and Z. Su, “Ultrafast laser-enabled optoacoustic characterization of three-dimensional, nanoscopic interior features of microchips,” *Ultrasonics* **146**, 107510 (2025).
- ¹³ J. Li, Z. Shan, and E. Ma, “Elastic strain engineering for unprecedented materials properties,” *MRS Bull.* **39**(2), 108–114 (2014).
- ¹⁴ J. Feng, X. Qian, C.-W. Huang, and J. Li, “Strain-engineered artificial atom as a broad-spectrum solar energy funnel,” *Nature Photon* **6**(12), 866–872 (2012).
- ¹⁵ P.R. Chidambaram, C. Bowen, S. Chakravarthi, C. Machala, and R. Wise, “Fundamentals of silicon material properties for successful exploitation of strain engineering in modern CMOS manufacturing,” *IEEE Trans. Electron Devices* **53**(5), 944–964 (2006).
- ¹⁶ G. Huang, A. Beccari, N.J. Engelsens, and T.J. Kippenberg, “Room-temperature quantum optomechanics using an ultralow noise cavity,” *Nature* **626**(7999), 512–516 (2024).
- ¹⁷ J. Puebla, Y. Hwang, S. Maekawa, and Y. Otani, “Perspectives on spintronics with surface acoustic waves,” *Applied Physics Letters* **120**(22), 220502 (2022).

- ¹⁸ R. Sano, Y. Ominato, and M. Matsuo, “Acoustomagnonic Spin Hall Effect in Honeycomb Antiferromagnets,” *Phys. Rev. Lett.* **132**(23), 236302 (2024).
- ¹⁹ Y. Tsaturyan, A. Barg, E.S. Polzik, and A. Schliesser, “Ultraslow nanomechanical resonators via soft clamping and dissipation dilution,” *Nature Nanotech* **12**(8), 776–783 (2017).
- ²⁰ V.V. Temnov, A. Alekhin, A. Samokhvalov, D.S. Ivanov, A. Lomonosov, P. Vavassori, E. Modin, and V.P. Veiko, “Nondestructive Femtosecond Laser Lithography of Ni Nanocavities by Controlled Thermo-Mechanical Spallation at the Nanoscale,” *Nano Lett.* **20**(11), 7912–7918 (2020).
- ²¹ A. Ghita, T.-G. Mocioi, A.M. Lomonosov, J. Kim, O. Kovalenko, P. Vavassori, and V.V. Temnov, “Anatomy of ultrafast quantitative magnetoacoustics in freestanding nickel thin films,” *Phys. Rev. B* **107**(13), 134419 (2023).
- ²² P. Varlamov, J. Marx, Y.U. Elgueta, A. Ostendorf, J.-W. Kim, P. Vavassori, and V. Temnov, “Femtosecond Laser Ablation and Delamination of Functional Magnetic Multilayers at the Nanoscale,” *Nanomaterials* **14**(18), 1488 (2024).
- ²³ Chemical Rubber Company, *CRC Handbook of Chemistry and Physics: A Ready-Reference Book of Chemical and Physical Data*, 82. ed., 2001–2002 (CRC Press, Boca Raton, 2001).
- ²⁴ H. Masumoto, H. Saito, Y. Murakami, and M. Kikuchi, “Crystal Anisotropy and Temperature Dependence of Young’s Modulus in Single Crystal of Nickel,” *Trans. JIM* **10**(2), 119–123 (1969).
- ²⁵ L.D. Landau, L.P. Pitaevskij, A.M. Kosevich, and E.M. Lifšic, *Theory of Elasticity: Volume 7*, 3rd ed (n.d.).
- ²⁶ G. Benetti, M. Gandolfi, M.J. Van Bael, L. Gavioli, C. Giannetti, C. Caddeo, and F. Banfi, “Photoacoustic Sensing of Trapped Fluids in Nanoporous Thin Films: Device Engineering and Sensing Scheme,” *ACS Appl. Mater. Interfaces* **10**(33), 27947–27954 (2018).
- ²⁷ M. Gandolfi, S. Peli, M. Diego, S. Danesi, C. Giannetti, I. Alessandri, V. Zannier, V. Demontis, M. Rocci, F. Beltram, L. Sorba, S. Roddaro, F. Rossella, and F. Banfi, “Ultrafast Photoacoustic Nanometrology of InAs Nanowires Mechanical Properties,” *J. Phys. Chem. C* **126**(14), 6361–6372 (2022).
- ²⁸ M. Gandolfi, M.E. Serrano Flores, J. Frantz, J. Myers, R. Bekele, J. Sanghera, A. Clabeau, N.M. Litchinitser, and M.A. Vincenti, “Dynamic light-driven metasurface: Harnessing quasibound states in the continuum for laser-induced selective crystallization,” *Phys. Rev. A* **110**(1), 013510 (2024).
- ²⁹ “COMSOL Multiphysics® www.comsol.com COMSOL AB, Stockholm, Sweden,” (n.d.).
- ³⁰ K.-Y. Chou, C.-L. Wu, C.-C. Shen, J.-K. Sheu, and C.-K. Sun, “Terahertz Photoacoustic Generation Using Ultrathin Nickel Nanofilms,” *J. Phys. Chem. C* **125**(5), 3134–3142 (2021).
- ³¹ K.J. Manke, A.A. Maznev, C. Klieber, V. Shalagatskyi, V.V. Temnov, D. Makarov, S.-H. Baek, C.-B. Eom, and K.A. Nelson, “Measurement of shorter-than-skin-depth acoustic pulses in a metal film via transient reflectivity,” *Applied Physics Letters* **103**(17), 173104 (2013).
- ³² V.V. Temnov, I. Razdolski, T. Pezeril, D. Makarov, D. Seletskiy, A. Melnikov, and K.A. Nelson, “Towards the nonlinear acousto-magneto-plasmonics,” *J. Opt.* **18**(9), 093002 (2016).
- ³³ A. Kimel, A. Zvezdin, S. Sharma, S. Shallcross, N. de Sousa, A. García-Martín, G. Salvan, J. Hamrle, O. Stejskal, J. McCord, S. Tacchi, G. Carlotti, P. Gambardella, G. Salis, M. Münzenberg, M. Schultze, V. Temnov, I.V. Bychkov, L.N. Kotov, N. Maccaferri, D. Ignatyeva, V. Belotelov, C. Donnelly, A.H. Rodriguez, I. Matsuda, T. Ruchon, M. Fanciulli, M. Sacchi, C.R. Du, H. Wang, N.P. Armitage, M. Schubert, V. Darakchieva, B. Liu, Z. Huang, B. Ding, A. Berger, and P. Vavassori, “The 2022 magneto-optics roadmap,” *Journal of Physics D: Applied Physics* **55**(46), 463003 (2022).

SUPPLEMENTARY MATERIAL

Supplementary Note 1 – Fabrication of nickel cavities

Freestanding nickel cavities were fabricated using a pulsed laser (EXPLA, 30ps @ 1064 nm, 10 Hz repetition rate) focused on 230 nm thick nickel thin film evaporated on top of a SiO₂ substrate using a 20 cm lens under an incident beam at 45 degrees impinging from the substrate side. The sample was scanned through the laser focus at a constant speed of 1 mm/s resulting in fabrication of lines of nearly identical structures separated by a distance on 100 micrometers (see Supplementary Figure S1). Several lines of structures were fabricated at different pulse energies (in the μ J) range controlled by a combination of a motorized λ -half plate and a polarizer.



Supplementary Figure S1. SEM image of nickel cavities fabricated with laser spallation with different fluences. The marked line is the line containing the cavities characterized in our work, including the cavity presented in Figures 2, 3 and the cavities presented in Supplementary Figure S6 in the main text.

Supplementary Note 2 – Sample preparation for SEM imaging

In Figure 1a of the main text, we show cross-sections of the film and the cavity imaged by using scanning electron microscopy (SEM). To perform these measurements, we have performed precision ion beam milling of the structure using focused ion beam (FIB) followed by high resolution SEM imaging of structure cross sections. Prior to FIB-cutting, spallation cavities have been covered with a thin layer of Pt, initially using electron beam-induced deposition followed by a thicker Pt layer deposited by ion-beam induced deposition. This step is essential for preventing the surface of the nickel film from damage during the thick protective Pt-layer deposition. Another advantage of using e-beam deposited Pt layer is that it provides good contrast at the interface of Ni-film and ion-deposited Pt layer. Both protective layers allow to preserve the initial surface and prepare a clean and sharp FIB cut. The SEM images of the cross-sections, presented in Figure 1a in the main text, were obtained using a HeliosNanoLab 450S (ThermoFisher) at the accelerating voltage of 2–5 kV and the beam current of 50-100 pA. From these images we can get information

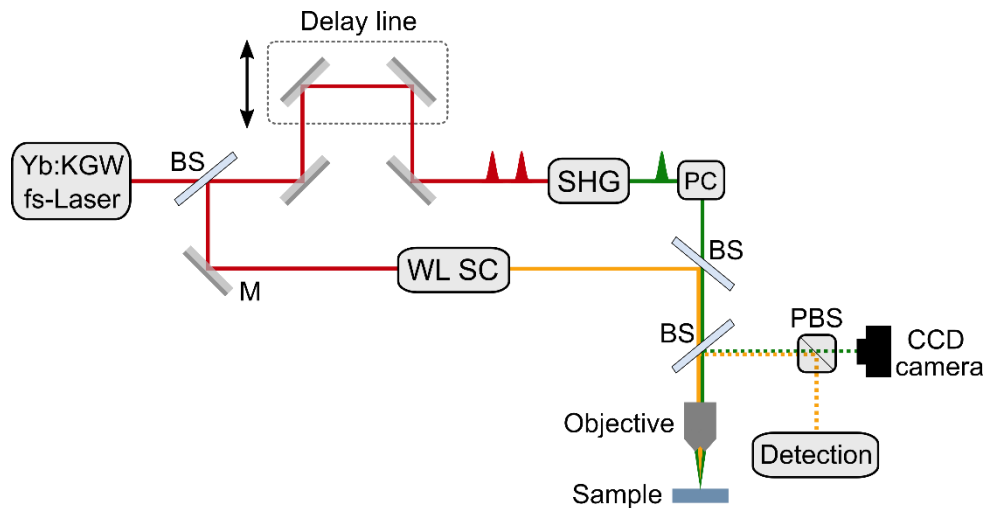
about the possible differences in the crystal structure after the laser spallation fabrication procedure.

Supplementary Note 3 – Pump-probe measurements

A first laser pulse (pump) is focused onto the sample and results in a thermally induced expansion that generates a time-dependent strain profile at the first interface (air/nickel) that travels back and forth within the nickel cavity/film, as sketched in Figure 1b. The propagation of this acoustic pulse can be studied using a second laser pulse (probe). Subsequent reflections of the acoustic pulse at the air/Ni interface are detected as a periodic modulation of the pump-probe transient reflectance signal $\Delta R/R$. The measured transient reflectance, that is the pump-induced reflectance change, is defined as

$$\frac{\Delta R}{R} = \frac{R_t - R_0}{R_0}$$

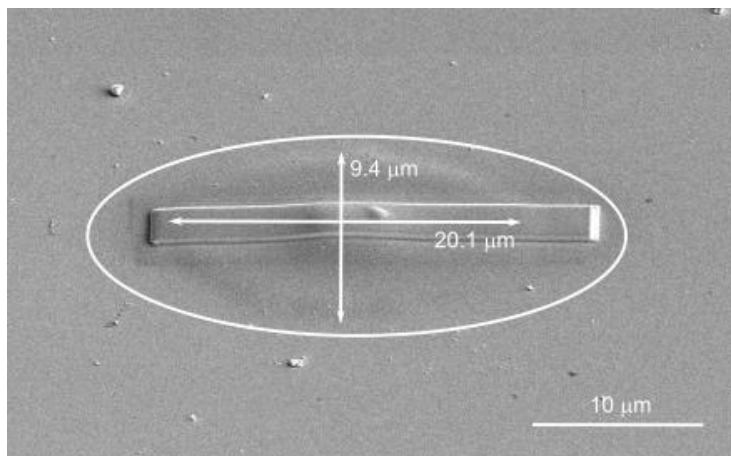
where R_t denotes the reflectance of the system after excitation and at a certain time delay between the pump and the probe pulses, while R_0 is the steady-state reflectance of the sample. The pump-probe setup, which is presented in Supplementary Figure S2, is based on an Yb:KGW laser system (Light Conversion®), delivering 220 fs pulses centered at 1030 nm with 500 mW average power at a repetition rate of 100 kHz. As illustrated in Supplementary Figure S2, a beam splitter (BS) divides the initial pulse train into two branches to form the pump and probe lines of our setup.



Supplementary Figure S2. Schematic representation of the setup used to carry out the experiments. The laser is divided into two lines, to respectively drive the pump (green) and the probe (yellow) beams towards the sample to perform the pump-probe spectroscopy measurements. A reflective objective is used to focus the pump and probe beams, as well as to image the sample onto a CCD camera. The reflected probe beam is filtered from the pump using a polarizing beam splitter (PBS) and detected by a photodiode. Acronyms: beam splitter (BS), mirror (M), white light supercontinuum (WL SC), Pockels cell (PC), second harmonic generation (SHG).

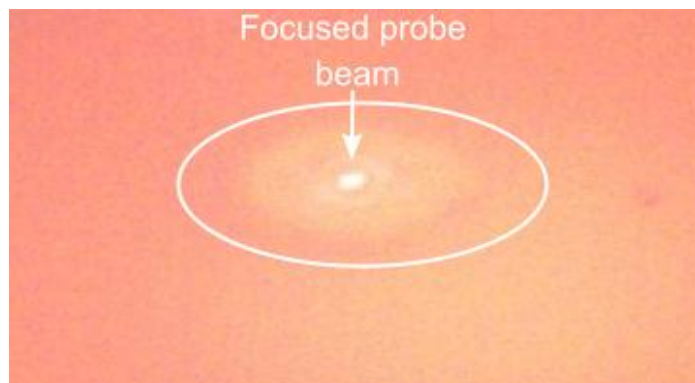
As pump beam, we use the second harmonic (SHG) of the laser fundamental (515 nm), modulated at half repetition rate, 50 kHz, using a Pockels cell (PC). The results shown here are performed with a pump fluence of 5 mJ/cm².

After excitation, the opto-mechanical dynamics is tracked by the probe beam, consisting of a white light supercontinuum (WLSC) generated using a YAG crystal and providing a broadband pulse from 500 to 950 nm with a duration of approximately 200 fs. The pump and probe beams are then focused onto the front size of the cavity at normal incidence by using a reflective objective (numerical aperture 0.5), to a spot size of approximately 20 μm for the pump beam and of 5 μm for the probe. Having a sufficiently small spot size is necessary to isolate the opto-acoustic response of a single cavity, which presents lateral dimensions in the range of 15 to 20 μm (see Supplementary Figure S3). The objective is also used to image the sample onto a CCD camera and verify that we are indeed pumping the center of the desired cavity structure (see Supplementary Figure S4). After interaction with the sample, the reflected probe beam is recollimated using the same objective, filtered from the pump using a polarizing beam splitter and detected by a photodiode. To minimize noise in the measurements and easily separate the signals from the two beams, pump and probe polarizations are set perpendicular to each other.

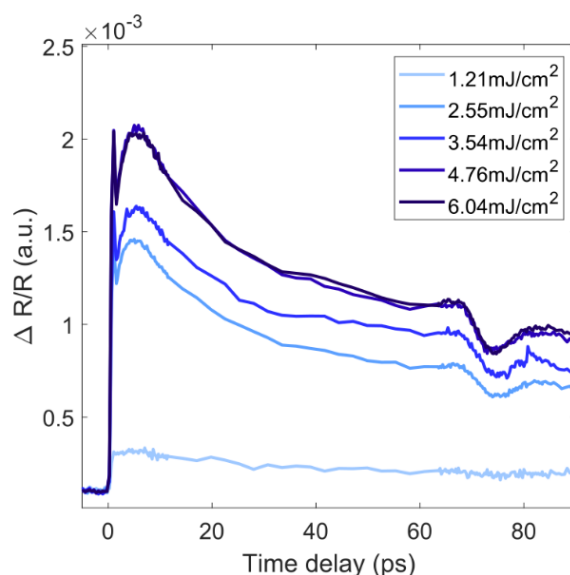


Supplementary Figure S3. Top-view SEM image of a nickel cavity, circled in white, indicating the lateral dimensions of the bubble. The rectangular structure on top is the Pt layer used to perform FIB and then SEM imaging of the vertical profile of the cavity.

Additional measurements at different fluence values are presented in Supplementary Figure S5, as well as on different cavities to check the reproducibility of the results reported in the main text on different cavities fabricated under the same conditions (see Supplementary Figure S6, the cavity discussed in the main text is also included in – red curve – as reference). As it can be noticed, for a delay of 480 ps we can observe a similar number of acoustic echoes and time delay in which they appear.

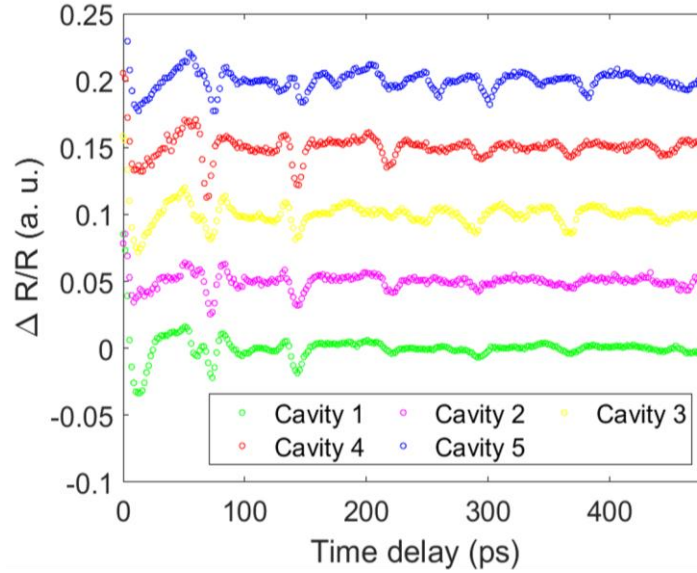


Supplementary Figure S4. Top-view of a cavity taken with the reflective objective use in the experimental setup with the probe beam at the center of the cavity. The circle represents the lateral dimensions of the cavity, proving that we are probing the center of the structure.



Supplementary Figure S5. Pump-probe measurements at different fluence values. Saturation is reached for a fluence close to 5 mJ/cm².

Slight differences between the opto-acoustic response of the different cavities can be attributed to a difference in the change of the crystal structure during fabrication and therefore in the acoustic response. Also, there might be intrinsic damping (i.e., viscoelasticity, defects, etc.), that may be random on different cavities. Thus, more optimization studies are needed to control the microstructure and roughness of the produced membranes to allow for a good reproducibility of the structures, although this goal is outside the scope of the current work.



Supplementary Figure S6. Transient reflectance measurements of 5 nominally identical cavities, fabricated under the same conditions.

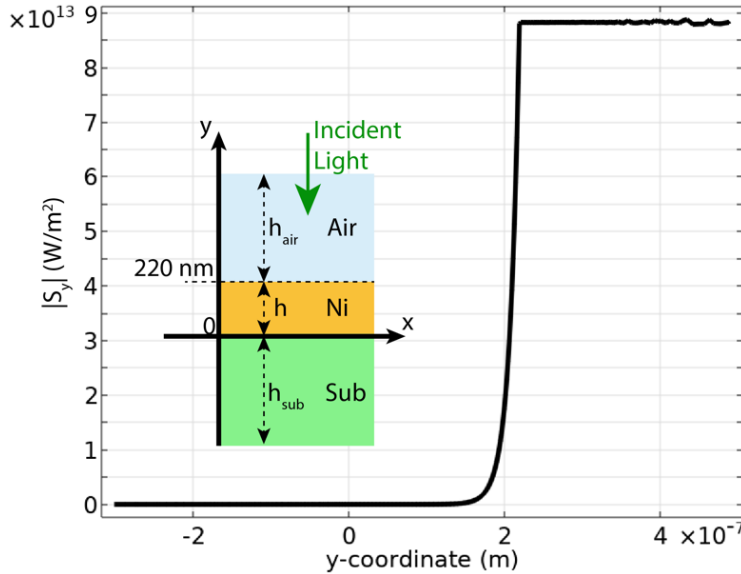
Supplementary Note 4 – Details on numerical simulations

We have developed an opto-thermo-mechanical multi-physics model, that has been solved with Finite Elements Method (FEM) implemented in COMSOL Multiphysics®. The model solves three physical processes (optical, thermal and mechanical) sequentially. The solution of each step is used to compute the next one. The system under consideration is a Ni layer of thickness $h = 220$ nm, sandwiched among a semi-infinite air domain and a substrate (that may be either air – for the cavity – or glass – for the film case). Since in the experiment the pump beam size exceeds the one of the probe, the latter can be considered to measure the system in a region where the excitation intensity is maximum and rather homogeneous. Thus, it is reasonable to approximate the probed part of the system as a 1D system (along y coordinate – propagation of both the pump pulse and the acoustic longitudinal wave excited by the pump beam) since the dependence on the x and z coordinates is a constant. Within this approximation, the excitation can be well approximated by a plane wave propagating towards negative y -direction and whose intensity matches the pump beam peak intensity. The temporal period on one optical cycle is below 2 fs, way faster than the duration of the pulse. For this reason, it is enough to consider a frequency domain approach rather than a transient analysis for the optical part of our numerical analysis. To exploit the potentialities offered by COMSOL Multiphysics®, the aforementioned geometry has to be cast into a 2D geometry (x - y coordinates), see the inset of Supplementary Figure S7. By doing so, the translational invariance along the z -axis is automatically enforced. Furthermore, to model the translational invariance along x -direction, periodic boundary conditions (BC) are applied on the sides perpendicular to the x -axis for all the considered physics. With this approach, the choice of the domain width along x does not influence the results (even if we fixed the latter geometrical parameter to be as the light wavelength, for numerical convenience).

Optical part. Three domains are considered, one for the air ($n = 1$), on top of the Ni layer of thickness h (with $n = 1.85$ and $k = 3.4 @515 \text{ nm}^1$), anchored to a substrate (either $n = 1$ for the cavity or $n = 1.45$ for the film), see the inset of Supplementary Figure S7 for a sketch. The top air domain height is fixed to $h_{air} = 300 \text{ nm}$, and it is truncated with a perfectly matched layer (PML) to approximate it as semi-infinite and avoid spurious reflections. The substrate domain height is $h_{sub} = 300 \text{ nm}$ as well, and it is truncated with a scattering BC. Despite the latter avoids spurious reflections to mimic a semi-infinite substrate, this choice is irrelevant because no light is transmitted to the substrate due to the high absorption of the Ni layer. As anticipated, the pump is modeled as a plane wave, and introduced with a periodic port. In the experiment, the pump wavelength, FWHM temporal duration, and fluence are $\lambda = 515 \text{ nm}$, $\tau = 200 \text{ fs}$ and $\Phi = 5 \text{ mJ/cm}^2$, respectively. Therefore, the intensity of the plane wave is as the peak intensity of the pump pulse (we refer to Ref. [2] for further details):

$$I_0 = \sqrt{\frac{4 \ln(2) \Phi}{\pi}} \frac{\Phi}{\tau} \approx 23.5 \frac{\text{GW}}{\text{cm}^2}. \quad (S1)$$

The mesh size was set as 1/10 of the wavelength in each domain, whereas it was smaller than 4 nm in the Ni layer, to carefully follow the electric field exponential decay.



Supplementary Figure S7. Absolute value of the Poynting vector, y component, vs y. Inset: scheme of the 2D geometry used for the FEM.

The Maxwell's equations were solved with a frequency domain study (Electromagnetic Waves, Frequency Domain module was used), and the fields were calculated everywhere.

Hence, it is possible to calculate the dissipated power per unit volume due to Ohmic losses as:

$$Q_h(\mathbf{r}) = \frac{1}{2} \text{Real}(\mathbf{J} \cdot \mathbf{E}^*) = \frac{1}{2} \omega \varepsilon_0 \text{Imag}(\varepsilon_r) |\mathbf{E}(\mathbf{r})|^2, \quad (S2)$$

where \mathbf{J} is the total current density, \mathbf{E} is the electric field, $\omega = 2\pi/\lambda$ and ε_r the complex relative permittivity. Since the imaginary part of ε_r is 0 for air and glass, losses are present in the Ni nickel domain only. The solution of the optical problem disclosed a light reflection of 62.4% at the air-Ni interface, whereas the remaining 37.6% is absorbed within the top part of the Ni layer. In Supplementary Figure S6 we report the Poynting vector as a function of y , showing an exponential decay within the first 30 nm (i.e. the skin depth) of the Ni layer. No transmission is recorded to the substrate, both for the cavity and the film. In accordance with the Poynting vector profile, the absorbed optical power is confined within the top part of the Ni layer.

Thermal part. Once the optics has been solved, the thermal dynamics is considered. Since the pulse is 200 fs long, energy is delivered to the electronic population of the Ni layer, and only on later times energy is exchanged with the phonons. Hence a Two Temperature Model (TTM) is appropriate to describe this situation. The implemented equations are:

$$C_e \frac{\partial T_e}{\partial t} = \kappa_{T,e} \nabla^2 T_e + Q(\mathbf{r}, t) - G_{ep}(T_e - T_p), \quad (S3)$$

$$C_p \frac{\partial T_p}{\partial t} = \kappa_{T,p} \nabla^2 T_p + G_{ep}(T_e - T_p), \quad (S4)$$

where T_e and T_p are the electronic and phononic temperatures, respectively, G_{ep} is the electron-phonon coupling coefficient, $\kappa_{T,e}$ and $\kappa_{T,p}$ are the electronic and phononic thermal conductivities, respectively, C_e and C_p are the electronic and phononic specific heat per unit volume, respectively. The system was initially at rest, so $T_e = T_p = T_0 = 293.15$ K everywhere. At later times, the pump pulse excites the system. The temporal duration of the excitation, not considered for the optics analysis, is now introduced by assigning a volumetric heat source term with a Gaussian temporal shape:

$$Q(\mathbf{r}, t) = Q_h(\mathbf{r}) \exp \left[-4 \ln(2) \frac{(t - t_0)^2}{\tau^2} \right], \quad (S5)$$

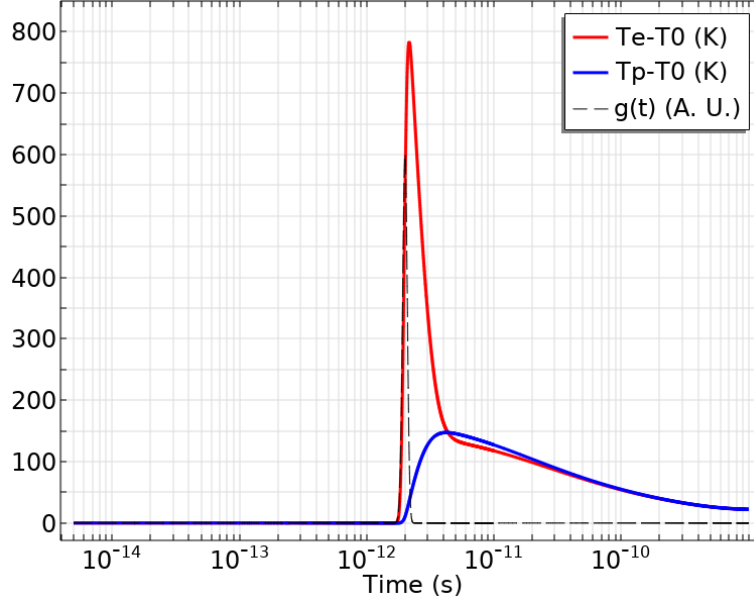
where $Q_h(\mathbf{r})$ was calculated previously with the optics step, τ is the pulse temporal FWHM, and the time maximizing the light intensity is $t_0 = 10\tau$ to avoid conflicts with the initial conditions. For the cavity, equations S4 and S5 have been solved only within the 220 nm thick Ni layer, the presence of the air being neglected. On the Ni-air surfaces, adiabatic BCs were imposed both for

both the temperatures. No free electrons are available in the air, so they cannot carry any energy flux. As for the phonons, the air thermal conductivity is quite low, of the order of (or lower than) $10^{-2} \text{ W m}^{-1}\text{K}^{-1}$, and on the considered time scales it does not play. However, to be on the safe side, we have also tried to replace the adiabatic BCs for the phononic heat flux with radiative and convective BCs, but no significant changes on the obtained temperature profile were observed.

As for the film, we have also considered the SiO_2 substrate anchored to the bottom side of the Ni layer. The substrate is insulator, with no free electrons available. Hence, Eq. S3 was solved only in the Ni layer. Adiabatic BCs for the electronic heat flux were applied to both the Ni layer boundaries perpendicular to y . On the other hand, heat transfer to the substrate through phonons may occur, so Eq. S4 was solved also for the substrate. On the external boundaries perpendicular to y coordinate adiabatic BCs for the phononic heat flux were enforced. The substrate height is $h_{sub} = 8 \text{ }\mu\text{m}$, hence in the time range of interest (1 ns after the arrival of the pump pulse), the thermal dynamics does not reach the end of the SiO_2 domain. As a result, the temperature profile obtained is equivalent to that of an infinite substrate, and the choice of the BC on the lower boundary of the substrate does not alter the result. The mesh adopted for the optics was replicated in the Ni layer and its proximal substrate. In the bottom part of the substrate, where no interesting dynamics occurs, the mesh was progressively released to reduce the numerical burden. As for the temporal step, to follow the pulse carefully, a temporal step of 10 fs was used. For times longer than 10 ps, the temporal step was released to 1 ps, to reduce the computational burden. The used thermal properties are summarized in Supplementary Table ST1. Eqs. S3 and S4 were solved together at the same time, with a time dependent study. Two coupled Heat transfer in Solid physics were implemented in COMSOL Multiphysics. The result consists in the two-temperature spatial and temporal profiles. In Supplementary Figure S8 we report the electronic and phononic temperature vs time in proximity of the top surface of the Ni layer, for the cavity. Since the thermal conductivity of the glass is very low, the heat flow to the substrate is very inefficient and the temperature profile in Ni layer in the simulated time range for the film case is very similar to the one obtained for the cavity. At 1 ns, the temperature increase in the top part of the substrate is as low as 20 K.

Supplementary Table ST1. Thermal parameters used in our analysis. The parameters for Ni are taken from Ref. [3]. Despite the precise value of these parameters may vary depending on the sample, they are somehow consistent also with what reported in Refs. [4,5].

Thermal parameter	Value
$\kappa_{T,e}$ in Ni	$(0.2 \text{ W m}^{-1}\text{K}^{-2}) \times T_e$
C_e in Ni	$\gamma_e T_e = (1077 \text{ J m}^{-3}\text{K}^{-2}) \times T_e$
$\kappa_{T,p}$ in Ni	$20 \text{ W m}^{-1}\text{K}^{-1}$
C_p in Ni	$3.63 \times 10^6 \text{ J m}^{-3}\text{K}^{-1}$
G_{ep} in Ni	$8.55 \times 10^{17} \text{ W m}^{-3}\text{K}^{-1}$
$\kappa_{T,p}$ in SiO_2	$0.8 \text{ W m}^{-1}\text{K}^{-1}$
C_p in SiO_2	$1.76 \times 10^6 \text{ J m}^{-3}\text{K}^{-1}$



Supplementary Figure S8. Electronic (red) and phononic (blue) temperature increase vs time (horizontal axis, log scale). The temperatures were calculated at the coordinate $y = h - 10$ nm. The temporal shape of the pulse (black dashed line) has been reported for the sake of comparison.

Acoustic part. For this step we consider the same geometry, mesh and temporal discretization already described for the thermics. The acoustics rely on the solution of Navier's equation:

$$\rho \frac{\partial^2 \mathbf{u}}{\partial t^2} = \nabla \cdot \sigma, \quad (S6)$$

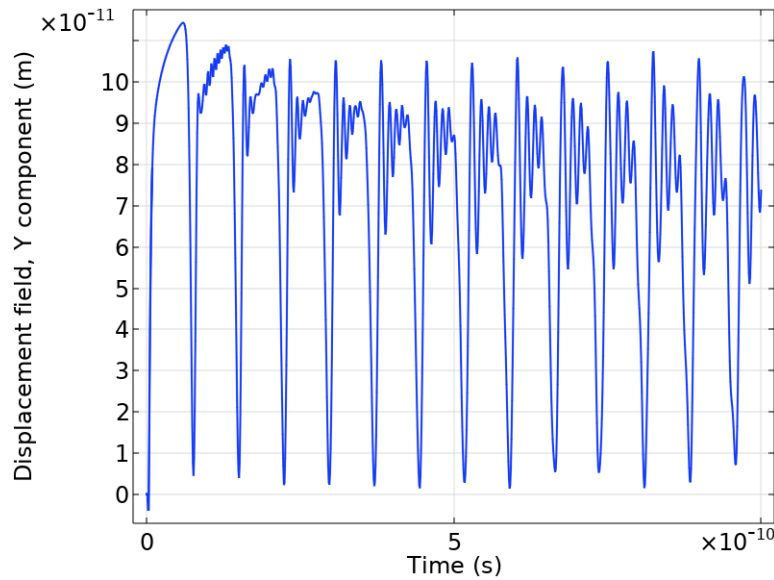
$$\sigma = C : (\varepsilon - \alpha \Delta T_p I), \quad (S7)$$

where \mathbf{u} , σ , C , ε , ρ , α and I are the displacement, the stress, the stiffness tensor, the strain, the mass density, the linear expansion coefficient, and the identity matrix, respectively (we refer to Ref. [2] for further details). ΔT_p is the phononic temperature increase calculated previously with the thermics. The initial conditions are rest, i.e., $\mathbf{u}(t = 0) = \mathbf{0}$ and $\frac{\partial \mathbf{u}}{\partial t}(t = 0) = \mathbf{0}$. We enforced free boundary conditions on both the external boundaries perpendicular to y . In the case of the film, the substrate is long enough so that the lower boundary does not influence the result in the computed time interval, as if the substrate were semi-infinite. The parameters used for this computation are summarized in Supplementary Table ST2. The acoustics has been modeled in COMSOL Multiphysics® with a Solid Mechanics module and solved with a time dependent study. Due to the symmetry of the excitation and of the geometry, only the longitudinal component of the displacement (u_y) is going to play. The displacement as a function of time, calculated in proximity of the Ni layer top surface, is reported in Supplementary Figures S9 and S10 for the cavity and the film, respectively. As we may see, in both the cases we see several displacement dips, each one arriving ~ 73 ps after the previous. These dips correspond to the acoustic echoes. For the case of

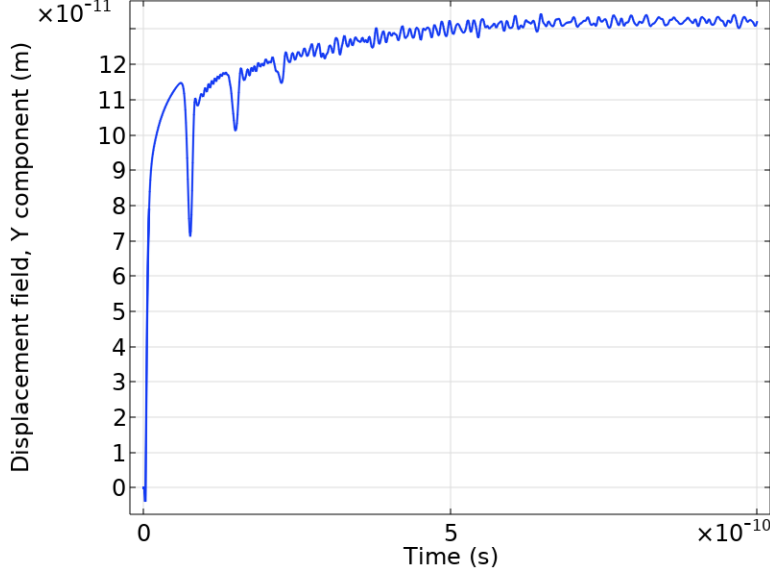
the film, the amplitude of the dips decreases with time, a signature of the extrinsic damping related to the mechanical energy transfer to the substrate occurring along with every reflection at the lower boundary of the Ni layer. On the other hand, in the case of the cavity, the dips amplitude mainly remains constant with time, since no other damping mechanisms have been introduced in the model.

Supplementary Table ST2. Acoustic parameters used in our analysis. We used the parameters of Polycrystal Ni and fused silica (for the substrate), that are isotropic materials. The stiffness tensor components and mass densities are taken from Ref. [6]. The thermal expansion coefficients are taken from Refs. [7,8] for Ni, and Refs. [9,10] for fused silica.

Acoustic parameter	Polycrystal Ni	SiO ₂
C_{11} [GPa]	324.0	78.5
C_{44} [GPa]	80.0	31.2
ρ [kg m ⁻³]	8900	2200
α [K ⁻¹]	15.0×10^{-6}	0.5×10^{-6}



Supplementary Figure S9. Displacement u_y as a function of time for the cavity. The displacement was calculated at the coordinate $y = h - 10$ nm from the nickel/air interface.



Supplementary Figure S10. Displacement u_y as a function of time for the film. The displacement was calculated at the coordinate $y = h - 10$ nm from the nickel/air interface.

We pinpoint the fact that for both the cavity and the film the displacement is expected to be periodic in time as it can be represented as a superposition of the fundamental mode with a period $T_1 = \left(\frac{2h}{v_l}\right)$ and its higher harmonics with periods $T_n = T_1/n$:

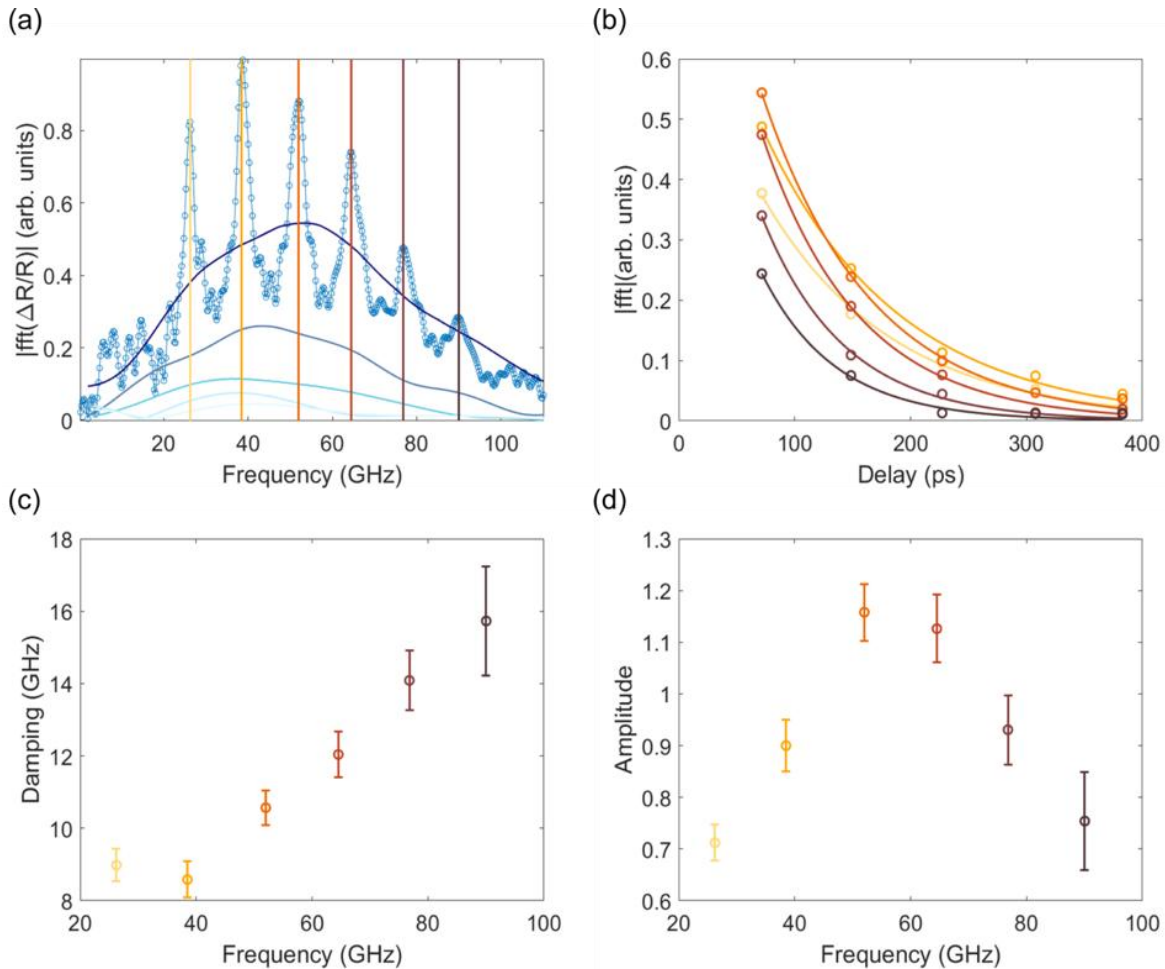
$$u_y(y, t) = \sum_{n=1}^{+\infty} A_n(y) \cos \left[2\pi \left(\frac{v_l}{2h} \right) nt + \phi_n \right].$$

However, in Figure S10 we plot the displacement in the first ns after excitation. If we look at Figure S8, it is clear that within 1 ns the system is not yet thermalized, and so we expect the echoes to become “perfectly” periodic only after 1 ns, approximately after 10 ns after pump pulse excitation. Our intention was to show that in the case of a suspended cavity the number of echoes is much larger (infinite in the ideal case) compared to the case where the substrate takes part of the energy of the acoustic envelope every roundtrip, and so the number of echoes is much less (see Figure S9).

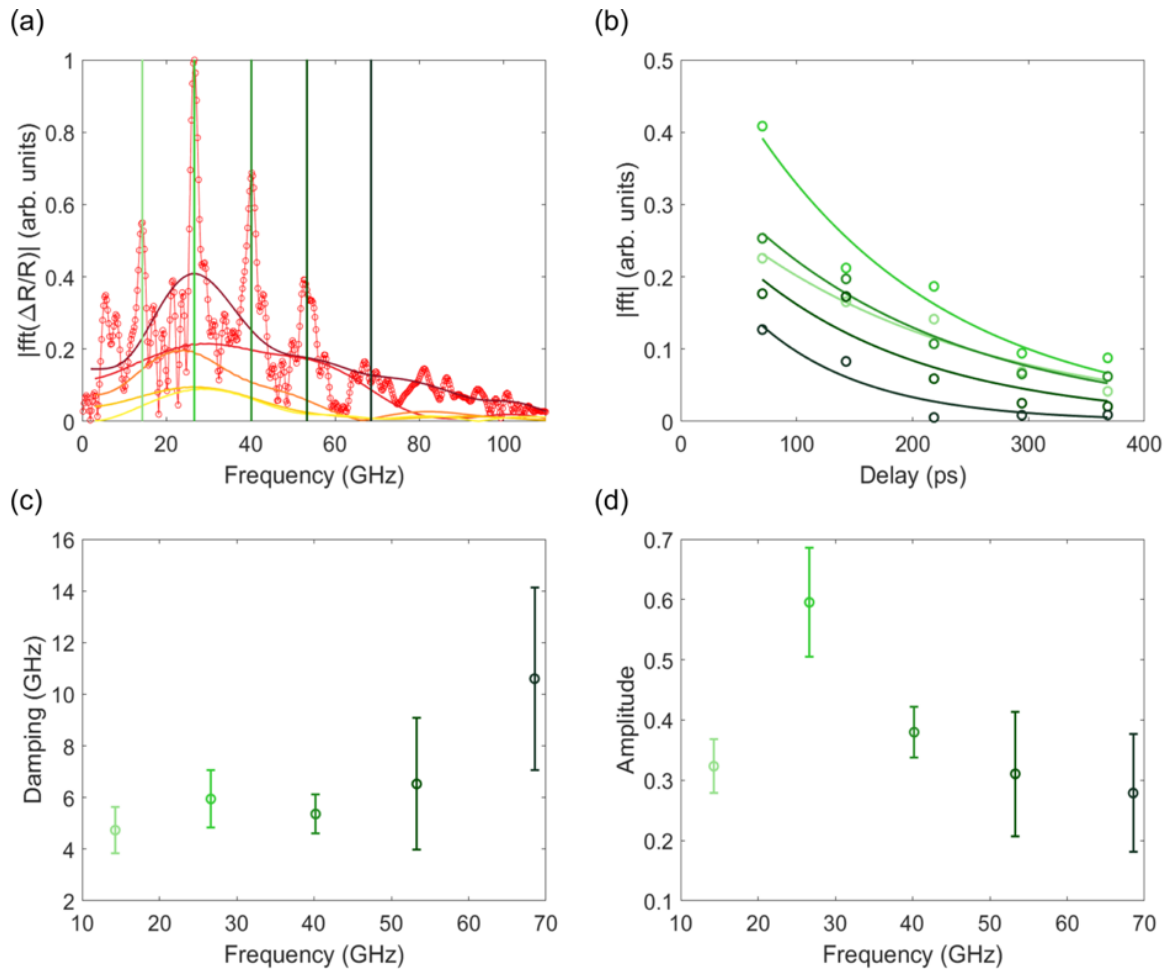
Supplementary Note 5 – Details on the Fourier analysis of the single echoes

In this note we provide more details on the analysis of how damping and amplitude presented in Figure 3 in the main text were obtained. In Supplementary Figures S11a and S12a we plot the FFT of full temporal traces (Figure 2c,d in the main text) together with the FFT of the isolated first five echoes of both film and cavity (Figure 3a,b in the main text). The individual echoes are isolated by setting a time interval centered around the minimum peak of each echo. The time interval was varied until we obtained a stable FFT for each echo. The resulting FFT spectra are normalized to the sum of the FFT of all the selected echos (in the revised version we considered five echos in

total). We have extracted the points cut by the same frequencies for the six film eigenmodes and the five cavity ones (corresponding to the eigenfrequencies calculated in the main text and represented in Figure 3c,d by stars), and fitted them with a first order exponential (see Supplementary Figures S11b and S12b). From this fit we obtained both damping, and amplitude represented in the main text in Figure 3c,d, respectively, as well as the error bars, which are obtained directly from the fit (see also Supplementary Figures S11c,d and S12c,d).



Supporting Figure S11. (a) FFT of the temporal trace (Figure 3b) and the first four echoes for the film. (b) Amplitude of the FFT of the first four echoes at different frequencies as a function of the time delay. The continuous line is the exponential fit from which we extract damping (c) and amplitude (d) of the eigenmodes. The data in (c) and (d) are the blue points in Figure 3c and 3d, respectively, in the main text.



Supporting Figure S12. (a) FFT of the temporal trace (Figure 3b) and the first four echoes for the cavity. (b) Amplitude of the FFT of the first four echoes at different frequencies as a function of the time delay. The continuous line is the exponential fit from which we extract damping (c) and amplitude (d) of the eigenmodes. The data in (c) and (d) are the red points in Figure 3c and 3d, respectively, in the main text.

Supplementary References

¹ P. Johnson, and R. Christy, “Optical constants of transition metals: Ti, V, Cr, Mn, Fe, Co, Ni, and Pd,” *Phys. Rev. B* **9**(12), 5056–5070 (1974).

² M. Gandolfi, S. Peli, M. Diego, S. Danesi, C. Giannetti, I. Alessandri, V. Zannier, V. Demontis, M. Rocci, F. Beltram, L. Sorba, S. Roddaro, F. Rossella, and F. Banfi, “Ultrafast Photoacoustic Nanometrology of InAs Nanowires Mechanical Properties,” *J. Phys. Chem. C* **126**(14), 6361–6372 (2022).

³ K. Kang, and G.-M. Choi, “Thermal coupling parameters between electron, phonon, and magnon of Nickel,” *Journal of Magnetism and Magnetic Materials* **514**, 167156 (2020).

⁴ Z. Lin, and L.V. Zhigilei, “Temperature dependences of the electron–phonon coupling, electron heat capacity and thermal conductivity in Ni under femtosecond laser irradiation,” *Applied Surface Science* **253**(15), 6295–6300 (2007).

⁵ Z. Tong, S. Li, X. Ruan, and H. Bao, “Comprehensive first-principles analysis of phonon thermal conductivity and electron-phonon coupling in different metals,” *Phys. Rev. B* **100**(14), 144306 (2019).

⁶ B.A. Auld, *Acoustic Fields and Waves in Solids. 1* (Wiley, New York, 1973).

⁷ R.N. Abdullaev, Yu.M. Kozlovskii, R.A. Khairulin, and S.V. Stankus, “Density and Thermal Expansion of High Purity Nickel over the Temperature Range from 150 K to 2030 K,” *Int J Thermophys* **36**(4), 603–619 (2015).

⁸ T.G. Kollie, “Measurement of the thermal-expansion coefficient of nickel from 300 to 1000 K and determination of the power-law constants near the Curie temperature,” *Phys. Rev. B* **16**(11), 4872–4881 (1977).

⁹“Key Properties of Fused Silica,” (n.d.).

¹⁰“The engineering toolbox,” (n.d.).